Experimental determination of Pb partitioning between sulfide melt and basalt melt as a function of P, T and X

Stanley R. Hart*, Glenn A. Gaetani

Department of Geology and Geophysics, Woods Hole Oceanographic Institution
Woods Hole, Massachusetts 02543, United States

Abstract

We have measured the partition coefficient of Pb ($\underline{Kd^{Pb}}$) between FeS melt and basalt melt at temperatures of 1250° - 1523°C, pressures of 1.0 GPa – 3.5 GPa and oxygen fugacities at iron-wustite and wustite-magnetite. The total observed range of $\underline{Kd^{Pb}}$ is 4.0 – 66.6, with a strong negative dependence on pressure and a strong negative dependence on FeO of the silicate melt (Fe^{+2} only). The FeO control was constrained over a wide range of FeO (4.2% - 39.5%). We found that the effect of oxygen fugacity can be subsumed under the FeO control parameter. Prior work has established the lack of a significant effect of temperature (Kiseeva and Wood, 2015; Li and Audetat 2015). Our data are parameterized as: $\boldsymbol{Kd^{Pb} = 4.8 +(512 - 119*P \text{ in GPa})*(1/FeO – 0.021)}$. We also measured a single value of $\underline{Kd^{Pb}}$ between clinopyroxene and basalt melt at 2.0 GPa of 0.020 ± 0.001. This experimental data supports the "natural" partitioning of Pb measured on sulfide globules in MORB (Patten et al, 2013), but not the low Kd^{Pb} of ~ 3 inferred from sulfides in abyssal peridotites by Warren and Shirey (2012). It also quantitatively affirms the modeling of Hart and Gaetani (2006) with respect to using sulfide to buffer the canonical Nd/Pb ratio for MORB and OIB (Hofmann, 2003). For the low FeO and pressure of segregation typical of MORB, Kd^{Pb} ~ 45, and the Nd/Pb ratio of erupted basalts will be the same as the Nd/Pb ratio of the mantle source. The remaining puzzle is why MORB and OIB have the same Nd/Pb when they clearly have different FeO and pressure of melt segregation.

1. Introduction

Allegre (1969) first proposed using sulfide segregation into the core to solve the First Pb Paradox (The Pb isotopes in the sum of available earth reservoirs do not lie on the 4.56 Gy Bulk Earth isochron). This was amplified by Allegre (1982) and recently by Wood and Halliday (2005). Using Fe-rich sulfides as efficient Pb "getter" phases has also been advocated for some of the other paradoxes and enigmas that characterize Pb behavior in the earth (Hofmann, 1988; Hart and Gaetani, 2006). While some Pb partitioning data exists for mantle silicate phases (e.g. Hauri et al, 1994; Hart and Dunn, 1993), virtually no relevant data exists for Pb partitioning between sulfide and silicate phases. The first experimental studies were reported by Brenan and McDonough (2005) and Hart and Gaetani (2009), followed by several multi-parameter but largely isobaric studies by Li and Audetat (2012, 2015) and Kiseeva and Wood (2013, 2015). We show

here the importance of pressure in controlling Pb partitioning between sulfide melt and basaltic silicate melt, and present a simple parameterization that will cover most upper mantle basalt generation and differentiation processes.

2.1 Experimental Methods

Starting materials consisted of mixtures of 90% natural basalt and 10% high purity FeS with Pb added as either high purity PbO or PbS. Basalts used in this study were ALV-1690-20 (Grove et al., 1990) for run SPb-2, and AII0092-029-001(Ryan and Langmuir, 1987; Cottrell and Kelley, 2011) for all other runs, collected from 22.9167°N and 23.0438°N on the Mid-Atlantic Ridge, respectively. Major element data may be found in Appendix Table A.1. Starting materials were prepared by weighing out the components and grinding them under ethanol for thirty minutes using an agate mortar and pestle. The mixture was then dried down and homogenized for thirty minutes using a Wig-L-Bug.

All experiments were conducted using an end-loaded piston cylinder device with either 1.90 (SPb-2) or 1.27 cm diameter assemblies (Boyd and England, 1960). Experiment SPB-2 was conducted using an inner capsule fabricated from a single crystal of San Carlos olivine and a pressure-sealed Ni metal outer capsule (O'Leary et al., 2010). All other experiments were conducted using a graphite inner capsule and a pressure-sealed outer capsule fabricated from either Ni metal (SPb-4, -5) or fused quartz.
Experiments conducted at controlled f_{O_2} conditions used the following solid buffer assemblages placed below the sample in the graphite inner capsules: Fe^0 + FeO (iron–wüstite or IW), or FeO + Fe_3O_4 (wüstite–magnetite or WM). At the end of each experiment the presence of both components of the f_{O_2} buffer was verified by scanning electron microscopy. Experiments SPb-46, -48, and -55 were run in graphite capsules without a solid buffer.

All experiments were conducted using the cold-piston-in technique (Johannes et al., 1971). The friction correction was determined at 1.2 to 1.4 GPa and 1300 ºC using the breakdown of Ca-Tschermakite to the assemblage anorthite, gehlenite, and corundum (Hays, 1966) and is within the pressure uncertainty (±50 MPa). Therefore, no friction correction was applied to the reported pressures. Experiments were heated from room temperature to 1200 ºC at a rate of 1º C/s. The temperature was controlled using $W_{97}Re_3$-$W_{75}Re_{25}$ thermocouples with no correction for the effect of pressure on thermocouple EMF. The thermocouple bead was positioned 1 mm above the capsule and the temperature difference between the thermocouple tip and the center of the sample was determined to be 35 ºC using the method of Watson et al. (2002). Reported temperatures are corrected to reflect this offset. The accuracy for pressure is within ±50 MPa and for temperature is within ± 10 ºC. Experiments were terminated by turning off the power.

2.2 Analytical Methods – Electron microprobe

With one exception, run products were only two phases: basaltic glass and quench-textured iron sulfide. Run 12 had in addition a large crystal of clinopyroxene. The major element compositions of experimental run products were determined using the 5-

spectrometer JEOL JXA-8200 electron microprobe at the Massachusetts Institute of Technology. An accelerating voltage of 15 kV, beam current of 10 nA, and beam diameter of 20 μm was used for all glass analyses. Counting times were 5 s for Na and 40 s for all other elements. Data were reduced using a modified ZAF procedure (Armstrong, 1988). Quenched sulfides were analyzed using a large (~50 μm) beam to help average out the effects of quench growth.

2.3 Analytical Methods – LA-ICP-MS

Pb analyses in the experimental charges were performed at the Woods Hole Oceanographic Institution by either a New Wave 213 nm Nd-YAG laser or a 193 nm Excimer laser, with ablation products swept with He gas directly into a Thermo Scientific ELEMENT 2 ICP-MS. No inlet of liquid was involved, as this invariably raised the Fe and Pb backgrounds. Isotope masses ^{57}Fe, ^{206}Pb and ^{208}Pb were counted in medium resolution mode; comprehensive tests showed that isobaric interferences in this mode were inconsequential. Instrument set-up and tuning was done while lasering NIST SRM 610 glass. As Fe and Pb optimized at somewhat different settings, we strove for a "happy medium" between the two.

We found that run time, stability and precision were improved by using a raster analysis. This consisted of 4 lines 75 μm long, 25 μm apart, connected at the ends, run with a 25 μm spot, track speed 5 μm/s, 80% power at 20 Hertz. To clean any smearing of sulfide onto the basalt glass during polishing, we pre-ablated the pattern at 60% power, 25μm/s track speed at 10 Herz. During ablation, the signal was given 10-15 seconds to grow in and stabilize before data collection was started. Only three masses were collected sequentially during the run sequence (^{57}Fe, ^{206}Pb, ^{208}Pb).

The run protocol for each sample consisted of 2-3 backgrounds (gas blank, no laser), 2-5 runs on SRM 610 glass (until statistics were suitable), 2 runs on sample glass, 2-3 runs on sample sulfide, 1-2 runs on sample glass, gas blank, 2-3 runs on SRM 610 glass, 2 gas blanks, 20-30 minutes of clean-out, next sample started. Typical ^{57}Fe intensities (cps) were: 150-300 for gas blanks, 5000-8000 for SRM 610, >500,000 for sample glasses, > 2 million for sulfides. Typical ^{208}Pb intensities were 50-150 for gas blanks, 50,000-200,000 for SRM 610, >100,000 for sample glass, >2 million for sulfide. With a total time on each mass of ~ 20 seconds, total counts on standards and samples are sufficient for precisions of a few per mil. Actual in-run ratio statistics were of course lower than this.

A single shard of NIST SRM 610 was used for all of the sample analyses, re-polishing as necessary. Exterior edges were avoided, as Eggins et al (2002) showed that distinct heterogeneity exists in the NIST SRM glass series, particularly near the edges. Our work showed no evidence for any positional heterogeneity, and ^{208}Pb/^{57}Fe on raster spots at various places on the shard were repeatable to 2.2 %, for data taken over short time intervals (5-10 minutes, tested with 12 paired analyses). Ratio drift over periods of 8 hours could be 20-30%, and 610 was used to re-tune the operating parameters (typically the Ar gas flow rate). Drift corrections were made using the SRM 610 analyses; the ratio

versus time plots were smoothed with a 3rd order polynomials, with fits typically in the range 1-2%. Precisions of the sample glass $^{208}Pb/^{57}Fe$ ratios were typically somewhat better than the SRM 610 precisions. Precisions on the sulfides were generally worse, as the sulfides were always quench-textured, and signal fluctuations could be significant. Table 1 provides individual estimates of errors in the final Kd^{Pb} values.

2.4 Analytical Methods – Matrix effects on Fe and Pb ion yields

Obviously, ^{208}Pb intensity data alone on sample glass and quenched sulfide could be used to calculate a "raw" Pb partition coefficient. We found it clearly preferable to normalize the Pb intensities to those of Fe (whose concentrations were determined independently by electron probe for samples, and known from isotope dilution data for the 610 glass standard, and gravimetrically for the WHOI FeS 3000 ppm Pb standard). Comparisons showed differences of up to 30%, and the Fe-normalized data, especially for the quenched sulfide melt, was typically much more coherent. This was also clear from the chromatograms, that showed large intensity variations for Pb, but accompanied by coherent Fe variations.

There is an ever present concern in these kinds of partition experiments as to whether the laser ablation material has the same composition as the solid, and then whether the ion yield along the ion path is representative of both the ablation particle field and the solid starting material. It is a rare study that does more than assert that the ion ratios of two elements are independent of the matrix major element composition.

We have addressed this issue as follows. During one 5 hour analytical session, we inter-compared the $^{208}Pb/^{57}Fe$ ion ratio derived by lasering the NIST 610 glass standard with that derived by lasering a FeS pressed powder standard prepared at WHOI containing 3000 ppm Pb (the gravimetric powder mix was ground for 4 hours in alcohol). The Pb content of the 610 glass was determined originally by Tatsumoto by isotope dilution, with a value of 426 ± 1 ppm. The NIST certificate value for Fe is 458 ± 9 ppm, but given that this value dates to 1982 we felt a new look would be helpful. A fragment of our glass disc was analyzed by isotope dilution by Weiqiang Li and Clark Johnson at the University of Wisconsin, using the methods described by Beard et al (2003), and gave a value of 454.8 ± 3.3 ppm. The quality of the certified NIST value is impressive!

We show in Fig. 1 that the ion to weight ratio of $^{208}Pb/^{57}Fe$ are almost the same in the FeS and 610 glass standards. By doing a moving average interpolation scheme (e.g. each of the four FeS analyses at the beginning are compared to 610 values interpolated from the average of the first two runs and the following group of three runs, etc.), we find that the normalized $^{208}Pb/^{57}Fe$ ion ratio of the FeS standard is 1.11 ± 0.028 that of the 610 glass standard. Noting that intensities started to drop rapidly at around 280 minutes, we excluded the last three data points, with a resulting normalized $^{208}Pb/^{57}Fe$ ion ratio of FeS standard/610 glass standard of 1.070 ± 0.017. This is not statistically different from the result from the full data set, and the result is greater than 1.00 by 4σ. While this effect is small, it appears real and we have accordingly decreased our measured $^{208}Pb/^{57}Fe$ ion ratios in the sulfides by 7.0%.

3. Results: The dependence of Kd^{Pb} on P, T and X

A summary of run conditions and compositional data is given in Table 1. Sixteen successful runs were made at temperatures from 1250°C to 1523°C and pressures from 1.0 GPa to 3.5 GPa. Runs were buffered at iron-wustite, wustite-magnetite, or graphite buffered (maximum possible f_{O_2} corresponding to C-CO-CO_2). Electron probe analyses of silicate and sulfide phases are given in Appendix Table A.1. $Fe^{+2}O$ is calculated from FeO_{total} and equation 7 of Kress and Carmichael (1991). Typical run product photomicrographs are shown in Appendix Figures A.1., A.2., A.3. and A.4.

Three runs were analyzed in duplicate during separate LA-ICP-MS analytical sessions; see Table 1 and Figure 2. Duplicate analyses of run #2 agrees to ± 5%, and the duplicates of run #11 agree to ± 10%. The duplicate analyses of run #13 are different by a factor of two, and exhaustive consideration of the data did not provide any explanation. Later analysis of this sample by Sune Nielsen (for another purpose) shows that the high value is likely correct. Because this value also fits the regression line for the other 2.0 GPa data, we will disregard the low value, though admitting we have no obvious reason for doing so. We also note that runs #4 and #5 appear aberrant. These two runs were made in nickel containers, and the sulfide phase was very nickel-rich (57% and 79%); these runs are not considered further except to note that Pb appears to have a preference for FeS relative to NiS. Brenan (2015) also showed that Kd^{Pb} is lowered in high-nickel sulfides.

Run #12 lies off the plot but exactly on an extension of the 2.0 GPa isobar, at co-ordinates 66.63 and 0.241; the isobar through the five runs at 2.0 GPa is well-defined with a slope error of 3.3% (all regressions use the York (1966) two-error regression program). The runs at 3.0 and 3.5 GPa are virtually co-linear and provide a lower bound to the data. We have chosen to correct the 3.5 GPa value upwards by 16%, based on our parameterization given further below, to make it equivalent to 3.0 GPa data. While the 2.5 GPa runs are not spread out enough to constrain a regression line, we have chosen to pin the lower end of a logical line at the intersection of the 2.0 and 3.0 GPa regression lines (the intersection is at Y and X co-ordinates: 4.83 and 0.0209). A 1.0 GPa upper bound is fixed by fitting a line to runs #2 and #11. A summary of these regression fits is given in Table 2. Overall, it is clear that, at a given FeO content in the silicate melt, the Pb partition coefficient decreases with increasing pressure.

We have three cases where runs were buffered at both iron-wustite and wustite-magnetite. These may be compared in Table 1 and Fig. 2. At 2.0 GPa, #13 (I-W) is compared to #41 (W-M). The FeO is higher by 25% and the Kd is lower by 28% in the run buffered at W-M, thus the two points are spread along the 2.0 GPa line. At 2.5 GPa, #19 (I-W) is compared to #9 and #32 (W-M). Here the effect is not dramatic, but the Kd is lower in the two W-M runs. At 3.0 GPa, #15 (I-W) is compared to #33 (W-M). As at 2.0 GPa, the FeO is higher (by 23%) and the Kd is lower (by 19%) in the W-M buffered runs. The un-buffered runs (graphite only) are even lower in Kd than the W-M runs, suggesting these are more oxidized than W-M yet they still lie along the same 1/FeO lines. To generalize a bit, higher oxygen fugacity shifts some of the ferrous iron from the

sulfide melt into the silicate melt, while increasing the ferric/ferrous ratio in the silicate melt slightly. This increase in FeO leads to a decrease in Kd, in the same proportions as any change in FeO would due to bulk composition changes. In other words, there may be no direct effect of oxygen fugacity on Kd, but only through the change it drives in FeO content. This obviously simplifies the parameterization of Kd^{Pb}. Note that Li and Audetat (2012) suggest a correlation between oxygen fugacity and Kd^{Pb} (of order 7% decrease in Kd^{Pb} per log unit increase in fugacity), but the data are quite scattered, and statistically consistent with a zero effect.

The pressure dependence of the Pb partition coefficient can be visualized by calculating Kd^{Pb} at a given FeO content from each of the regression lines at 1, 2, 2.5 and 3 GPa (see Table 2). This is shown in Figure 3, for FeO contents of 8, 10 and 13%. The lines in pressure space appear to be linear, to first-order. Note that we are not able to separate temperature and pressure effects as we varied both together to keep the experimental conditions just above the liquidus for our bulk composition. The equivalent temperatures for each of the four plotted pressures in Figure 3 would be 1250°, 1370°, 1420° and 1475° C. Clearly the effect of temperature and/or pressure decreases as FeO increases, as is obvious from the fan-shaped isopleths in Fig. 3. We will show below that other studies have shown little or no temperature dependence of Kd^{Pb}.

4. Comparison with Literature Data

Kiseeva and Wood (2013) reported partitioning results for a wide variety of elements between sulfide melt and silicate melt. Their data are only for one temperature and pressure (1400°C, 1.5 GPa), but cover a similar range of silicate melt FeO as ours (2.9 – 40.1 %). Their range in FeO was intentional, while ours was somewhat serendipitous! Overall, their Kd^{Pb} shows a clear positive correlation with silicate melt 1/FeO, though with significant scatter due to a range of starting compositions and sulfide melt compositions. Excluding two CMAS compositions, and two high nickel sulfide compositions, their data show two clumps at FeO ~ 7.5% and FeO ~ 30%. Linear regression of these 15 runs (weighted with errors as stated in their Table 2 and 3) yields a fit: Kd = 300 (1/FeO) + 2.6, with a slope uncertainty of ± 12% (FeO here has been approximately corrected for 8% Fe^{+3}, using their delta FMQ ~ -1). This line lies between our 1.0 and 2.0 GPa lines in Fig. 2, consistent with the 1.5 GPa pressure of these runs. Reinforcing this agreement, when a Kd^{Pb} is calculated for 10% FeO from the regression line of the data of Kiseeva and Wood (2013), the result is Kd = 32.6 ± 1. This Kd^{Pb}, plotted on Figure 3 at 1.5 GPa, falls exactly on our FeO = 10% line.

Li and Audetat (2012) reported Kd^{Pb} data for a series of sulfide melt-silicate melt runs at 1.5 GPa over a temperature range of 1185° - 1300°C. The range in FeO was rather restricted (9.0 -11.9%), and there is no dependence of Kd^{Pb} on FeO apparent in the data. We have corrected their microprobe FeO_{total} data for Fe^{+3} (using their $Fe^{+3}$and oxygen fugacity data), and renormalized their FeO values for water contents (of up to 8%): the average of 11 runs at 1.5 GP is: FeO = 9.92%, Kd^{Pb} = 30.9 ± 3.4. We plot this average Kd^{Pb} in Figure 3 at 1.5 GPa, and it plots very close to our 10% FeO line (actually the point lies ~ 5% below our line, and is ~ 6% lower than the 1.5 GPa data of Kiseeva

and Wood(2013). Note the good agreement between Li and Audetat (2012) and Kiseeva and Wood (2013) despite the fact that there is more than 100°C difference between their respective run temperatures. The question of temperature dependence is expanded upon below.

Kiseeva and Wood (2015) reported a further series of studies specifically looking at the question of temperature dependence, and the compositional effect of Ni and Cu as significant components in the sulfide (as in Kiseeva and Wood 2013, all runs were at 1.5 GPa). They reported data for 6 runs in low Ni-Cu systems, at temperatures varying over a wide range (1300° - 1650°C). Five runs of similar FeO content (7.1 - 9.3%) showed a very limited, statistically insignificant range in Kd^{Pb}: 28.3 – 31.9. One high FeO run showed a lower Kd^{Pb} (9.6), but this is in line with the FeO control that we have discussed above. Kiseeva and Wood (2015) also give a parameterization that includes a temperature dependence, and this is seemingly contrary to the empirical evidence just discussed that showed no statistically significant temperature effect over a range of 350° C. Their parameterization would suggest a temperature effect on Kd^{Pb} of about a 10% decrease per 100°C temperature increase. A similar parameterization was given by Li and Audetat (2015), where the major control on Kd is through FeO, with temperature being only a minor control (Kd increases by ~ 5% per 100°C increase in temperature).

We will therefore proceed to parameterize our data with pressure and FeO as the major controls. While temperature is ignored in this parameterization, our runs contain an implicit P-T relationship based on the fact that our run conditions were chosen so as to lie ~ 35°C above the dry solidus of Katz et al (2003). The P-T equation for our run conditions is:

T°C = 110*P (in GPa) + 1146.

This relationship can be used to easily convert our parameterization from a pressure variable to a temperature variable. With either variable, our parameterization will be useful for situations such as generation of a sulfide melt/silicate melt pair along a peridotite solidus.

5. Parameterization

The equations for the regression fits in Table 2 and Fig. 3 are used to parameterize a general equation to calculate Kd's as a function of pressure and FeO content (note again that this is FeO *sensu stricto*, not FeO_{total}). As discussed above, the effects of oxygen fugacity may be accounted for in part by the FeO content – that is, variations in oxygen fugacity cause data points to move up or down the isobars in Fig. 2. The final equation is:

$$\boldsymbol{Kd^{Pb} = 4.8 + (512 - 119*P)*(1/FeO - 0.021),}$$

where P is in GPa, FeO is in weight percent (Fe^{+2} only), valid for $P \leq 3$ GPa. This equation returns values for each of our 13 runs between 4% and 21% FeO with a mean value of +0.3%, showing no sign bias in the parameterization. The absolute value of the deviation between measured Kd and calculated Kd ranges from 0.3% to 14%, with an average deviation of only 4.6%. This is only slightly larger than the average standard

error of the Kd measurements, which is 3.7% (see Table 1). Note that typical FeO_{total} values measured for basalts can be reduced by 8 – 10 % to provide $Fe^{+2}O$ values for the above equation.

Brenan (2015) reports a number of Kd^{Pb} values between sulfide and silicate melt, of which three are low-Ni sulfide and provide a test of our parameterization. The Kd's at 0.9 GPa range from 18.9 to 25.1, with quoted precisions of 2-5% (FeO values range from 18.6 to 20.9%, corrected to Fe^{+2} with data supplied in the paper). The Brenan values are higher than those calculated from our equation by 5%, 14% and 60%, and their range is clearly larger than is expected given the fairly narrow range in FeO.

While the parameterization of Li and Audetat (2015) is given as a power law between Kd and FeO, the curvature is imperceptible on our Kd versus 1/FeO plot. Furthermore, when their equation is compared to ours (above) at 1300°C and 1 GPa, the Kd's are very similar (<10%) over a useful range of FeO (5% - 15%). It is interesting to note that the Li and Audetat (2015) range in FeO was obtained by varying the starting compositions from basalt to rhyolite. Despite this huge range in bulk compositions, it appears possible to still account for the range in Kd^{Pb} by just one compositional parameter – FeO. Our parameterization (at 1.5 GPa) is consistently lower than that of Kiseeva and Wood (2015) at 1400°C by ~ 10-20 % (after an arbitrary 8% correction of their FeO parameter to Fe^{+2}). This appears inconsistent with the excellent fit of the Kiseeva and Wood (2013) data with ours, as shown in our Fig. 3.

Thus we argue that our parameterization given above will provide quantitative estimates for Kd^{Pb} over a wide range of P, T, fo_2 and composition.

6. Pb Partitioning between Clinopyroxene and Basalt Glass

Clinopyroxene appeared in only one of our runs, SPb-12. This cpx enclosed the sulfide and was in extensive contact with the silicate glass. A photomicrograph of this run is shown in Appendix Figure A.4. Pb partitioning data for our cpx/glass is given in Table 3. The Kd^{Pb} value of 0.020 ± 0.001 is in line with literature values, which range from 0.005 (Beattie 1993) to 0.058 (Adam and Green 2006), with intermediate values of 0.010 (Hauri et al 1994) and 0.028 (Schmidt et al 1999). A higher value of 0.13 is given by Klemme et al (2002), but this is for a cpx with relatively high Al_2O_3 content. Given the sulfide melt/silicate melt value of 67 measured in this run, the sulfide/cpx Pb partition value is very high, ~ 3315. So, for example, during partial melting of a peridotite with 10% modal cpx, it would only take a modal sulfide melt content of 0.003% to exert equal control on the bulk partitioning of Pb. This is in excellent accord with the models proposed by Hart and Gaetani (2006).

7. Comparisons with Natural Domains

Patten et al. (2013) analyzed sulfide droplets and coexisting MORB glasses to derive partition coefficients for 11 trace elements, including Pb. Pb contents ranged from 12 – 22 ppm in sulfide and 0.26 – 0.39 ppm in tholeiitic glass, with a relatively narrow

range of FeO contents in the glass (9.0 – 9.5 %). Kd^{Pb} values ranged from 45 – 73 (7 samples), and averaged 57. Our parameterization passes exactly through the average, if a ferric/ferrous ratio of 0.1 is assumed, and the pressure is taken to be 0 GPa. The fit at 1 GPa passes through the lowest point (Kd^{P} = 45), thus defining a lower bound to the data. Given the fast diffusion rates in sulfide and silicate glasses (Hart and Gaetani, 2006), it is sensible to expect phases in MORB to record very low pressures (magma storage typically at < 0.3 GPa). However, the highest Kd^{Pb} recorded in the Patten et al study (= 73) is difficult to reconcile with our equation, and suggests either melt phase disequilibria or some degree of analytical uncertainty. For example, at 0 GPa, a silicate melt FeO of 6.8% would provide the observed Kd^{Pb}, in contrast to the actual melt FeO of 9.1%. Perhaps the sulfide globules equilibrated in a somewhat evolved MORB melt, and were mixed into and quenched in the observed glass. This process would have to have been extremely rapid, given the fast diffusion coefficients for Pb in these melts.

Warren and Shirey (2012) looked at the other end of the melting domain, analyzing Pb by isotope dilution in sulfide grains picked out of 15 abyssal peridotites. Most of these peridotites were lherzolites, with only 3 harzburgites, thus we can presume only minor amounts of melt extraction prior to ridge emplacement. Pb contents in the sulfides ranged from 0.12 – 12.3 ppm, averaging 4.0 ppm. Except for one sample, all of these peridotite sulfides are lower in Pb than the sulfide melt globules of Patten et al (2013). This makes qualitative sense, if the basalt melts were generated at high pressure, low Kd^{Pb}, in equilibrium with sulfide melts at 4 ppm Pb, then transported to the surface where sulfides exsolve at low pressure and high Kd^{Pb}. This situation would be even more dramatic if the silicate melts are generated in equilibrium with a crystalline sulfide phase, where the Pb will be possibly even incompatible, as shown by Brenan (2015). So the mismatch between the Patten et al study and that of Warren and Shirey may be easily explainable, and thus the estimate by Warren and Shirey that sulfides contain only a small fraction of the depleted MORB mantle Pb budget may be valid. However, their estimate of a Kd^{Pb} of ~ 3, sulfide melt/silicate melt, is difficult to reconcile with any of the experimental Pb partitioning data discussed above. Experimental Kd^{Pb} values less than 10 only occur in silicate melts of extreme FeO contents (> 30%). As noted by Hart and Gaetani (2006), the sulfide liquidus is not well constrained in the pressure range of MORB generation and transport, so some of the equilibria may involve mixed sulfide solid and melt, possibly creating residues that look like low Kd^{Pb} histories.

Finally, we note that the detailed modeling done by Hart and Gaetani (2006) showed that a Kd^{Pb} of 44 would produce a horizontal (canonical) Nd/Pb array on a Hofmann plot, as advocated by Hofmann et al (1986) and Hofmann (2003) for a wide range of oceanic basaltic volcanics. In essence, the disparity in bulk silicate partition coefficients for Nd and Pb is brought into parity by adding in the sulfide partition component for Pb. A Kd^{Pb} of ~ 44 would suggest low FeO contents and low depths of magma segregation (as is typical for MORB), according to our parameterization. Thus such basaltic melts can be used to derive the Nd/Pb ratio of the mantle source for MORB, and this ratio is substantially higher than bulk-silicate earth values. The puzzle as to why MORB and OIB have the same Nd/Pb ratios remains, however, particularly when it is

noted that many OIB have high FeO and high depth of last equilibration (Hart and Jackson, 2014).

8. Closing Comment

All you need to know: $Kd^{Pb} = 4.8 + (512 - 119*P)*(1/FeO - 0.021)$

Acknowledgments

First and foremost, this work would not have been done without the support of NSF, through Grant EAR-0635530. Special thanks to Weiqiang Li and Clark Johnson at the University of Wisconsin for the isotope dilution analysis of Fe in the NIST SRM 610 glass standard. Mike Jercinovic at the University of Massachusetts wrung out his Ultrachron electron probe in developing a protocol to analyze Pb in silicate glass and sulfide quench product – the precision in glass looked good, the sulfur overlap in the sulfide was problematic. We thank Sune Nielsen for sharing his laser Pb data on re-runs of sample 13. Al Hofmann helped us orient our thinking by a masterful critique of our 2006 paper. The laser systems and both Element IIs were kept on good behavior, also ably resurrected from several spectacular crashes, by Jurek Blusztajn and Scot Birdwhistell. Finally, SRH acknowledges with great pleasure the years spent at MIT with Fred Frey as a colleague, wise mentor to students and provider of impeccable data.

References

Adam, J., & Green, T. (2006). Trace element partitioning between mica-and amphibole-bearing garnet lherzolite and hydrous basanitic melt: 1. Experimental results and the investigation of controls on partitioning behaviour. *Contributions to Mineralogy and Petrology*, *152*, 1-17.

Allegre, C. J. (1969). Comportement des systèmes U-Th-Pb dans le manteau supérieur et modèle d'évolution de ce dernier au cours des temps géologiques. *Earth And Planetary Science Letters*, *5*, 261-269.

Allègre, C. J. (1982). Chemical geodynamics. *Tectonophysics*, *81*, 109-132.

Beard, B. L., Johnson, C. M., Skulan, J. L., Nealson, K. H., Cox, L., & Sun, H. (2003). Application of Fe isotopes to tracing the geochemical and biological cycling of Fe. *Chemical Geology*, *195*, 87-117.

Beattie, P. (1993). The generation of uranium series disequilibria by partial melting of spinel peridotite: constraints from partitioning studies. *Earth and Planetary Science Letters*, *117*, 379-391.

458 Boyd, F.R., England, J.L. (1960). Apparatus for phase equilibrium studies studies at
459 pressures up to 50 kbar and temperatures up to 1750 °C. *J Geophys Res-Sol Ea 65*, 741-
460 748.
461
462 Brenan, J. M. (2015). Se–Te fractionation by sulfide–silicate melt partitioning:
463 Implications for the composition of mantle-derived magmas and their melting residues.
464 *Earth and Planetary Science Letters*, *422*, 45-57.
465
466 Brenan, J. M., & McDonough, W. F. (2005), Fractionation of highly siderophile elements
467 (HSEs) by sulfide-silicate partitioning: A new spin, *Eos Trans. AGU, 86*(52), Fall Meet.
468 Suppl., Abstract V41D-1502.
469
470 Cottrell, E., Kelley, K.A. (2011). The oxidation state of Fe in MORB glasses and the
471 oxygen fugacity of the upper mantle. *Earth and Planetary Science Letters 305*, 270-282.
472
473 Eggins, S. M., & Shelley, J. M. G. (2002). Compositional Heterogeneity in NIST SRM
474 610□617 Glasses. *Geostandards Newsletter*, *26*, 269-286.
475
476 Grove, T.L., Kinzler, R.J., Bryan, W.B. (1990). Natural and experimental phase relations
477 of lavas from Serocki Volcano, in: Detrick, R.S., Honnorez, J., Bryan, W.B., Juteau, T.
478 (Eds.), *Proceeding of the Ocean Drilling Program, Scientific Results*. Ocean Drilling
479 Program, College Station TX, pp. 9-17.
480
481 Hart, S. R., & Dunn, T. (1993). Experimental cpx/melt partitioning of 24 trace elements.
482 *Contributions to Mineralogy and Petrology*, *113*, 1-8.
483
484 Hart, S. R., & Gaetani, G. A. (2006). Mantle Pb paradoxes: the sulfide solution.
485 *Contributions to Mineralogy and Petrology*, *152*, 295-308.
486
487 Hart, S. R., & Gaetani, G. A. (2009). The solid earth Pb cycle, *Eos Trans. AGU, 90*(52),
488 Fall Meet. Suppl., Abstract V24A-01.
489
490 Hart, S. R., & Jackson, M. G. (2014). Ta'u and Ofu/Olosega volcanoes: the "Twin
491 Sisters" of Samoa, their P, T, X melting regime, and global implications. *Geochemistry,*
492 *Geophysics, Geosystems*, *15*, 2301-2318.
493
494 Hauri, E. H., Wagner, T. P., & Grove, T. L. (1994). Experimental and natural partitioning
495 of Th, U, Pb and other trace elements between garnet, clinopyroxene and basaltic melts.
496 *Chemical Geology*, *117*, 149-166.
497
498 Hays, J.F. (1966). Lime-alumina-silica. *Carnegie Institution of Washington Yearbook 65*,
499 234-239.
500
501 Hofmann, A. W. (1988). Chemical differentiation of the Earth: the relationship between
502 mantle, continental crust, and oceanic crust. *Earth and Planetary Science Letters*, *90*,
503 297-314.

Hofmann, A. W. (2003). Sampling mantle heterogeneity through oceanic basalts: isotopes and trace elements. In Holland H. D. and Turekian, K. K.(eds),*Treatise on geochemistry*, *2*, 61-101.

Hofmann, A. W., Jochum, K. P., Seufert, M., & White, W. M. (1986). Nb and Pb in oceanic basalts: new constraints on mantle evolution. *Earth and Planetary Science Letters*, *79*, 33-45.

Johannes, W., Bell, P., Mao, H.K., Boettcher, A.L., Chipman, D.W., Hays, J.F., Newton, R.C., Seifert, F. (1971). An interlaboratory comparison of piston-cylinder pressure calibration using the albite-breakdown reaction. *Contrib Mineral Petr 32*, 24-38.

Katz, R. F., Spiegelman, M., & Langmuir, C. H. (2003). A new parameterization of hydrous mantle melting. *Geochemistry, Geophysics, Geosystems*, *4*(9),1073, doi:10.1029/2002GC000433.

Kiseeva, E. S., & Wood, B. J. (2013). A simple model for chalcophile element partitioning between sulphide and silicate liquids with geochemical applications. *Earth and Planetary Science Letters*, *383*, 68-81.

Kiseeva, E. S., & Wood, B. J. (2015). The effects of composition and temperature on chalcophile and lithophile element partitioning into magmatic sulphides. *Earth and Planetary Science Letters*, *424*, 280-294.

Klemme, S., Blundy, J. D., & Wood, B. J. (2002). Experimental constraints on major and trace element partitioning during partial melting of eclogite. *Geochimica et Cosmochimica Acta*, *66*, 3109-3123.

Li, Y., & Audétat, A. (2012). Partitioning of V, Mn, Co, Ni, Cu, Zn, As, Mo, Ag, Sn, Sb, W, Au, Pb, and Bi between sulfide phases and hydrous basanite melt at upper mantle conditions. *Earth and Planetary Science Letters*, *355*, 327-340.

Li, Y., & Audétat, A. (2015). Effects of temperature, silicate melt composition, and oxygen fugacity on the partitioning of V, Mn, Co, Ni, Cu, Zn, As, Mo, Ag, Sn, Sb, W, Au, Pb, and Bi between sulfide phases and silicate melt. *Geochimica et Cosmochimica Acta*, *162*, 25-45.

Mengason, M. J., Candela, P. A., & Piccoli, P. M. (2011). Molybdenum, tungsten and manganese partitioning in the system pyrrhotite–Fe–S–O melt–rhyolite melt: impact of sulfide segregation on arc magma evolution. *Geochimica et Cosmochimica Acta*, *75*, 7018-7030.

O'Leary, J.A., Gaetani, G.A., Hauri, E.H. (2010). The effect of tetrahedral Al^{3+} on the partitioning of water between clinopyroxene and silicate melt. *Earth and Planetary Science Letters 297*, 111-120.

Patten, C., Barnes, S. J., Mathez, E. A., & Jenner, F. E. (2013). Partition coefficients of chalcophile elements between sulfide and silicate melts and the early crystallization history of sulfide liquid: LA-ICP-MS analysis of MORB sulfide droplets. *Chemical Geology*, *358*, 170-188.

Ryan, J.G., Langmuir, C.H. (1987). The systematics of lithium abundances in young volcanic rocks. *Geochim Cosmochim Acta 51*, 1727-1741.

Schmidt, K. H., Bottazzi, P., Vannucci, R., & Mengel, K. (1999). Trace element partitioning between phlogopite, clinopyroxene and leucite lamproite melt. *Earth and Planetary Science Letters*, *168*, 287-299.

Warren, J. M., & Shirey, S. B. (2012). Lead and osmium isotopic constraints on the oceanic mantle from single abyssal peridotite sulfides. *Earth and Planetary Science Letters*, *359*, 279-293.

Watson, E.B., Wark, D.A., Price, J.D., van Orman, J.A. (2002). Mapping the thermal structure of solid-media pressure assemblies. *Contrib Mineral Petr 142*, 640-652.

Wood, B. J., & Halliday, A. N. (2005). Cooling of the Earth and core formation after the giant impact. *Nature*, *437*, 1345-1348.

York, D. (1966). Least-squares fitting of a straight line. *Canadian J. Physics*, *44*, 1079-1086.

Figure Captions

Figure 1. Effect of matrix on ion yields of two standards. $^{208}Pb/^{57}Fe$ isotope ratio data, normalized to the established Pb/Fe ratios for two standards – NIST SRM 610 glass and a WHOI gravimetric FeS pressed powder standard. Note that actual isotopic compositions were used to calculate abundances of ^{208}Pb in the two standards; the accepted value of 2.119 % for ^{57}Fe was used for both standards. Data was taken on Oct. 23, 2008 with a 213 nm laser and our normal analysis protocol. Statistical analysis of this data shows that the $^{208}Pb/^{57}Fe$ ion yield ratio in the FeS standard is 1.070 ± 0.017 times that in the NIST SRM 610 standard (±1σ standard error). Due to a decaying signal, the last 3 data points were not utilized.

Figure 2. Pb partition coefficient between sulfide melt and silicate melt as a function of the inverse FeO content of the silicate melt (wt.% FeO *sensu stricto*, calculated using equation 7 of Cress and Carmichael, 1991). Run numbers are plotted next to each point, see Table 1 for run data. Earlier work has shown a strong tendency for the partitioning of Pb between FeS and silicate melt to correlate with 1/FeO of the silicate melt; this was first noted by Hart and Gaetani, 2009 and confirmed by Kiseeva and Wood (2013) and Li and Audetat (2015). Three isobars are shown, for runs at 1.0 GPa (dashed), 2.0 GPa

595 (blue) and 3.0/3.5 GPa (red). Run 12 plots exactly on the 2.0 GPa line, but is off the plot
596 at 1/FeO = 0.241.
597
598 **Figure 3.** Pb partition coefficient between sulfide melt and silicate melt, as a function of
599 pressure (GPa). From the regression equations for the four isobars (Table 2), Kd's were
600 calculated at FeO contents of 8, 10 and 13%. These Kd's are plotted here versus pressure,
601 for each of the three FeO contents (Fe^{+2} only). The arrays for the pressure dependence of
602 Kd^{Pb} are basically linear, and are fit with a York two-error regression program. At high
603 pressure, the regression lines have been extended beyond the actual data to emphasize the
604 convergence effect. The upper **X** is calculated for FeO = 10% from the regression of 15
605 runs at 1.5 GPa, from the experiments of Kiseeva and Wood (2013). The lower **X** is the
606 average of 11 runs at 1.5 GPa from the experiments of Li and Audetat (2012); the
607 average FeO was 9.92%. Clearly these two points at 1.5 GPa are in excellent agreement
608 with our FeO = 10% isopleth.

Appendix Figure Captions

Fig. A.1. Run SPb-5. Photomicrograph of run SPb-5, showing graphite inner capsule (fibrous texture), silicate glass (featureless gray) and Fe sulfide (bright blobs, mostly attached along glass-graphite boundary).

Fig. A.2. Run SPb-5. Enlarged view of the sulfide blob at the top edge of previous photo, diameter about 160 microns. Sulfide shows microcrystalline quench texture, as it was not possible to quench the sulfide to a glass.

Fig. A.3. Run SPb-13. In this run, the sulfide is largely contained in two blobs, attached to the side of the graphite capsule. The remainder of the capsule is basaltic glass, showing horizontal decompression cracks.

Fig. A.4. Run SPb-12. Clinopyroxene lines the bottom of the graphite container, and encloses the largest blob of sulfide. The rest of the capsule is featureless basaltic glass.

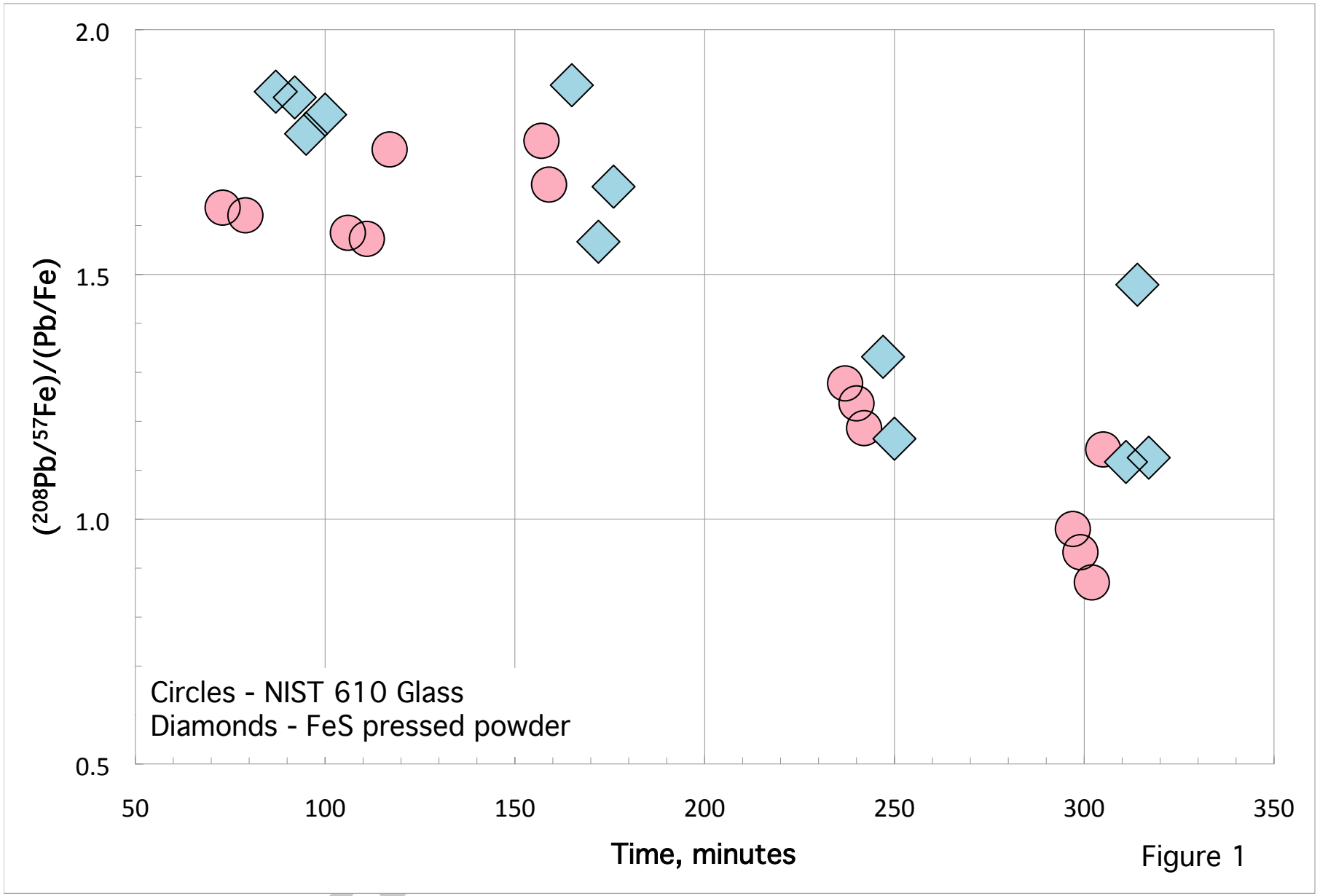

Figure 1

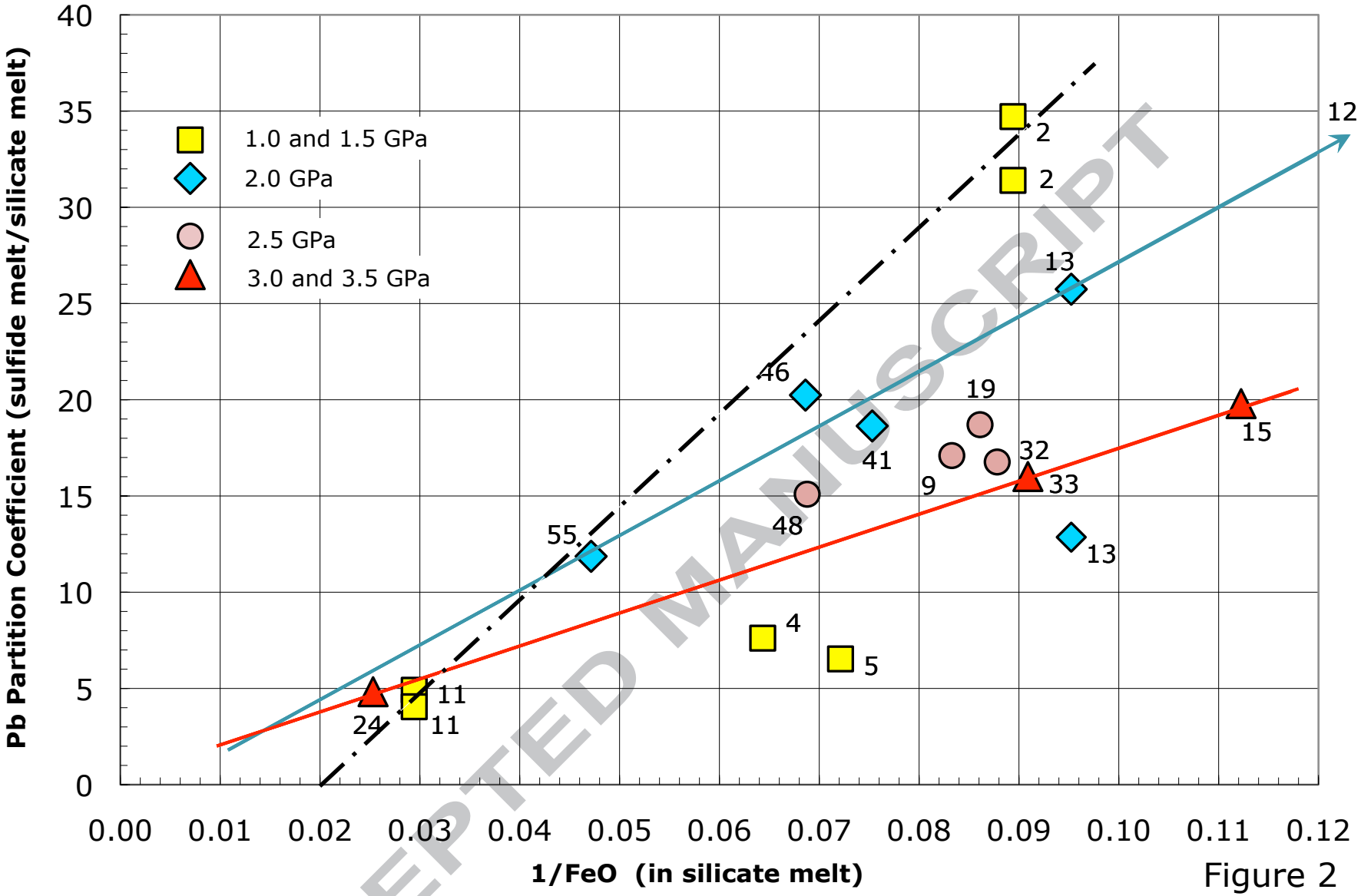

Figure 2

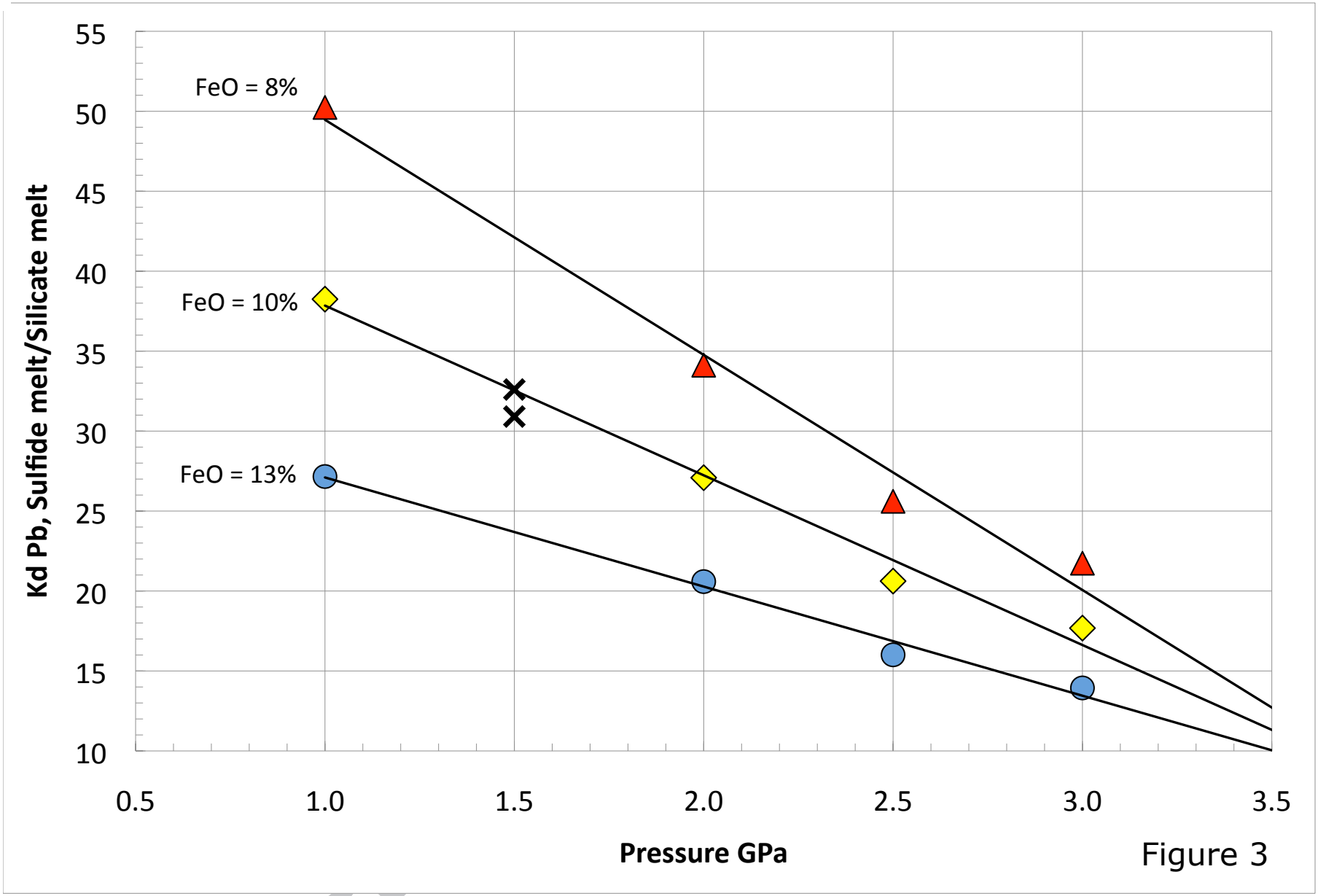

Figure 3

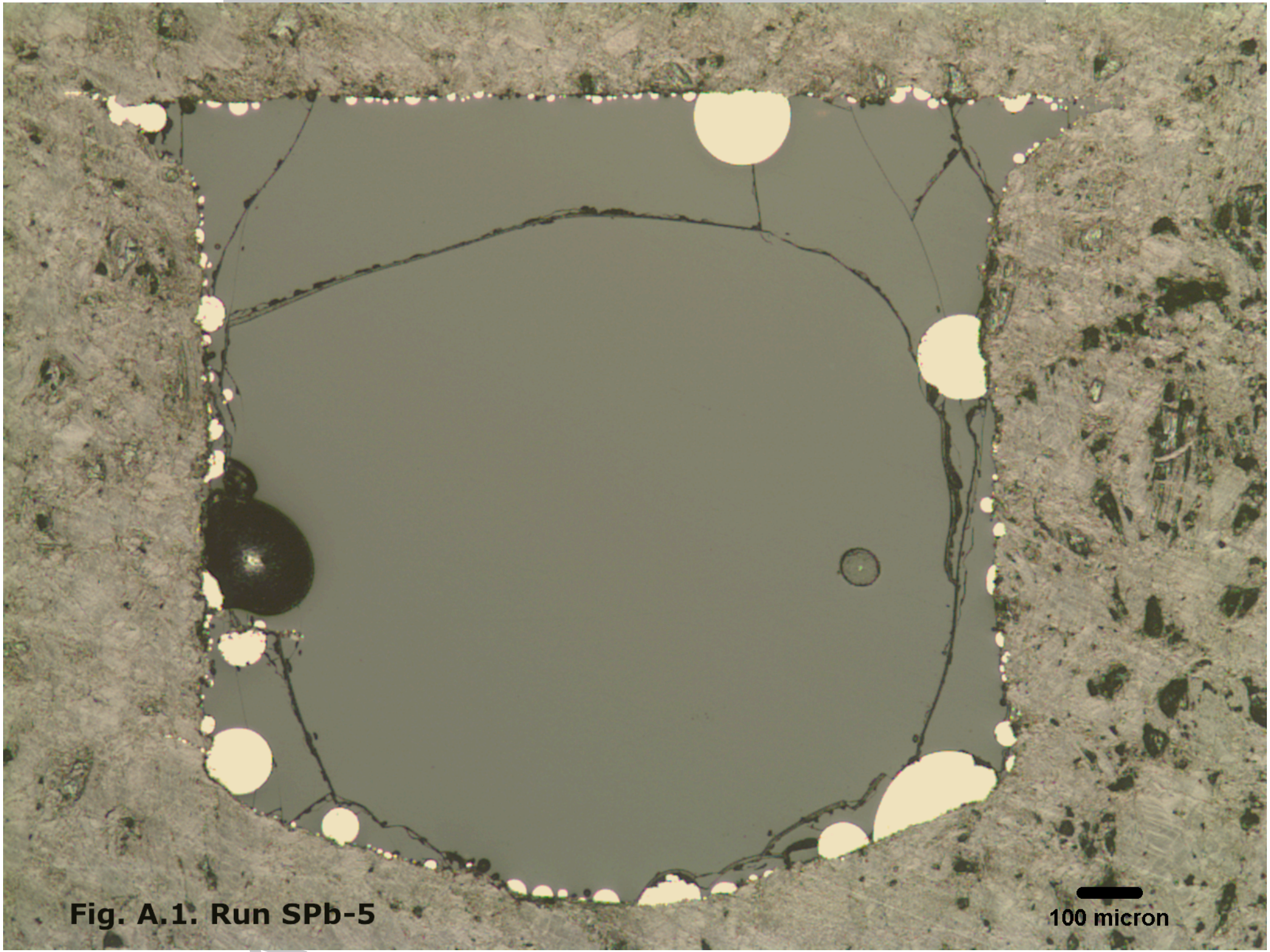

Fig. A.1. Run SPb-5

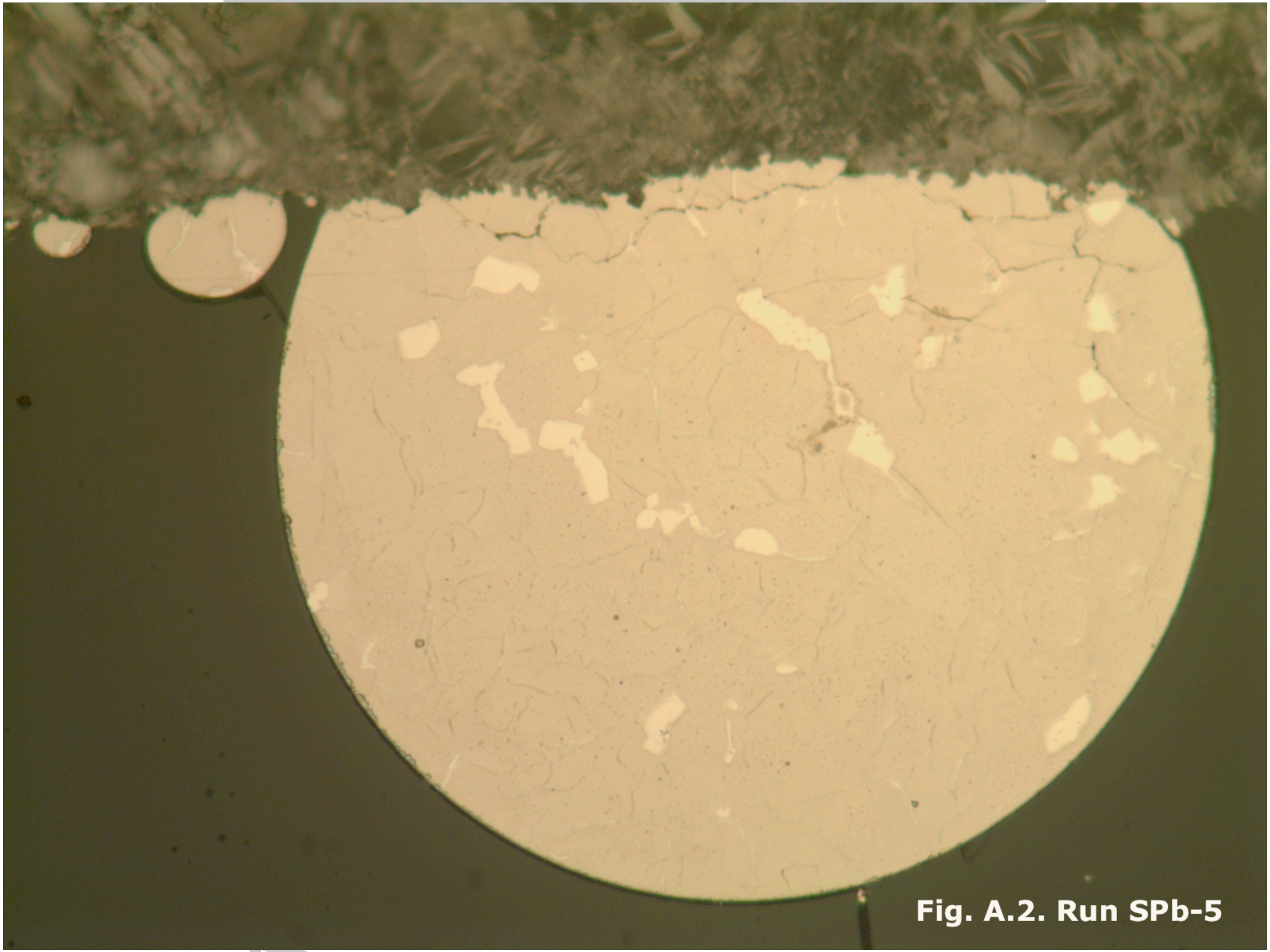

Fig. A.2. Run SPb-5

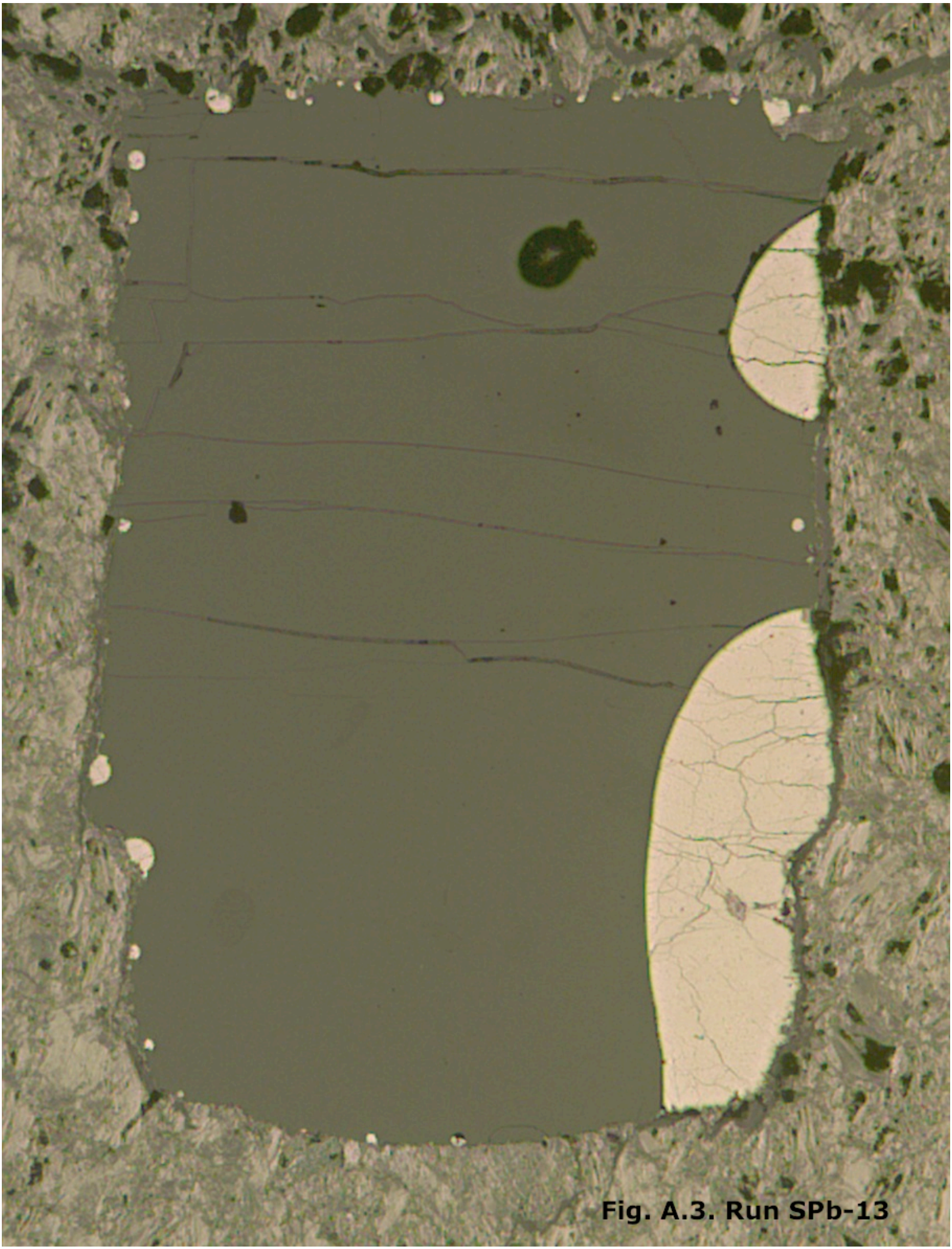

Fig. A.3. Run SPb-13

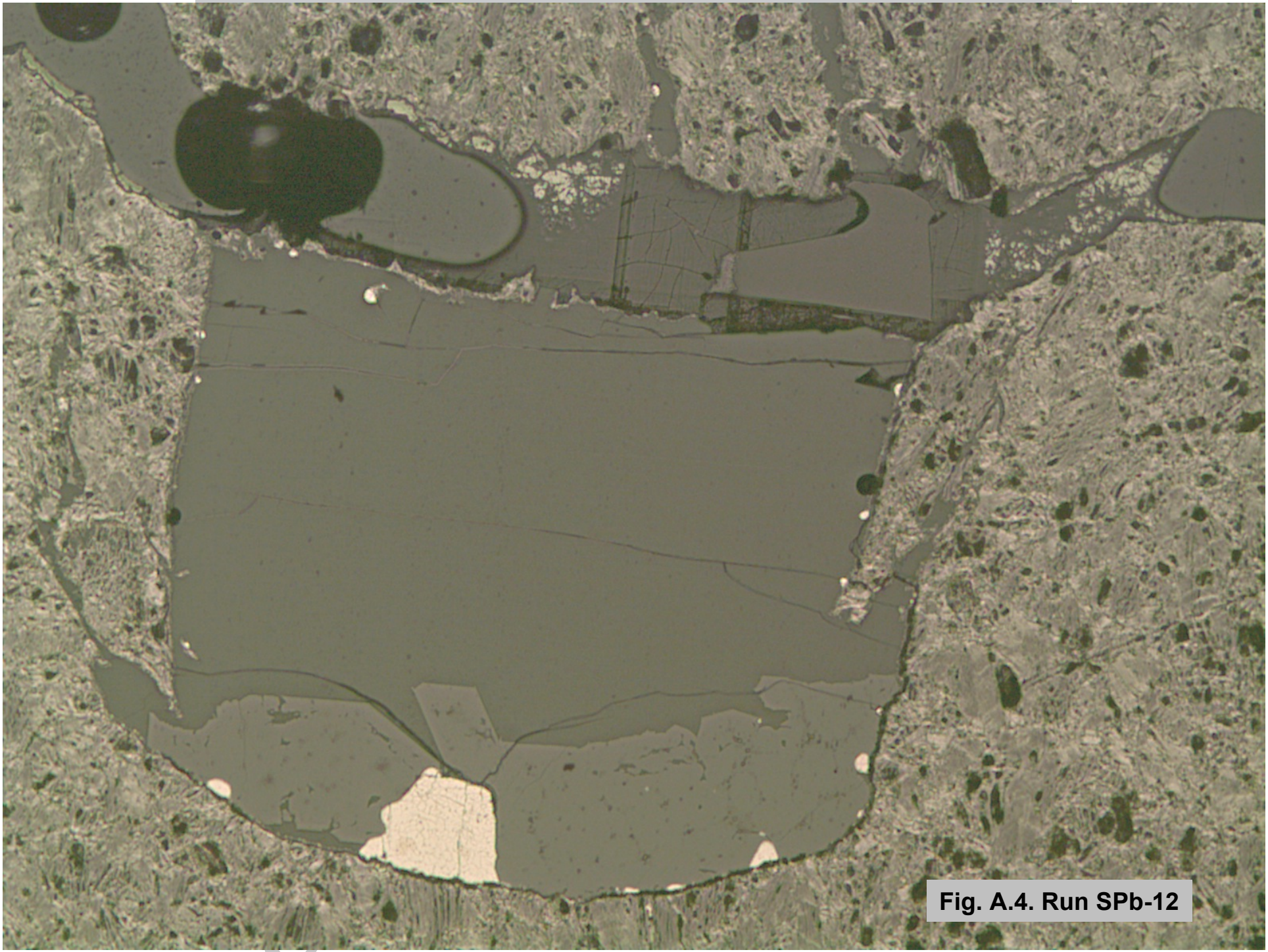

Fig. A.4. Run SPb-12

Table 1. Run Conditions, Selected Major Element Data and Pb partitioning Data for Sulfide Quench and Siliucate Glasses

	Temp	Pressure	**Kd Pb**	**Kd Pb**	Pb, %	Pb, ppm	Fe_2O_3	FeO	1/FeO	S	Fe	Ni	S	O	Fe+Ni	S+O	
Run No.	ºC	Gpa	**sul/sil**	**s.e. %**	sulfide	glass	glass	glass	glass	glass	sulfide	sulfide	sulfide	sulfide	sulfide	sulfide	Run No.
SPb-2	1300	1.0	**34.71**	**3.5**	7.488	2157	1.44	11.19	0.0894	0.442	57.43	1.07	34.83	3.84	58.50	38.66	SPb-2
SPb-2	1300	1.0	**31.40**	**2.7**	5.255	1674	1.44	11.19	0.0894	0.422	55.77	1.07	35.42	3.69	56.84	39.11	SPb-2
SPb-4	1250	1.0	**7.61**	**4.3**	1.179	1548	1.71	15.54	0.0643	0.004	4.32	78.5	19.04	0.38	82.86	19.42	SPb-4
SPb-5	1310	1.5	**6.53**	**20.1**	0.597	914	1.58	13.86	0.0721	0.039	17.19	57.3	27.57	0.69	74.48	28.26	SPb-5
SPb-9	1420	2.5	**17.10**	**2.9**	1.968	1151	1.43	12.01	0.0833	0.130	62.42	0.20	35.08	2.86	62.62	37.94	SPb-9
SPb-11	1250	1.0	**4.91**	**6.6**	0.609	1241	2.21	33.97	0.0294	0.450	68.07	0.30	30.37	2.88	68.37	33.26	SPb-11
SPb-11	1250	1.0	**4.05**	**10.1**	0.319	788	2.21	33.97	0.0294	0.450	68.07	0.30	30.37	2.88	68.37	33.26	SPb-11
SPb-12	1370	2.0	**66.63**	**2.7**	2.057	309	0.67	4.15	0.2410	0.081	64.21	0.20	32.87	1.09	64.41	33.96	SPb-12
SPb-13	1370	2.0	**25.74**	**2.9**	1.998	776	0.27	10.50	0.0952	0.157	61.28	0.19	34.84	2.85	61.47	37.69	SPb-13
SPb-13	1370	2.0	**12.86**	**2.7**	1.047	815	0.27	10.50	0.0952	0.157	61.28	0.19	34.84	2.85	61.47	37.69	SPb-13
SPb-15	1475	3.0	**19.80**	**1.3**	1.650	833	0.21	8.91	0.1122	0.158	68.50	0.16	30.33	1.14	68.65	31.47	SPb-15
SPb-19	1420	2.5	**18.71**	**6.7**	1.995	1067	0.27	11.61	0.0861	0.170	61.14	0.08	34.85	2.10	61.22	36.94	SPb-19
SPb-24	1523	3.5	**4.83**	**3.3**	0.571	1183	0.45	39.50	0.0253	0.620	71.83	0.11	25.41	1.66	71.94	27.07	SPb-24
SPb-32	1420	2.5	**16.77**	**4.2**	2.049	1222	1.40	11.39	0.0878	0.150	61.54	0.27	34.89	2.52	61.81	37.41	SPb-32
SPb-33	1475	3.0	**16.01**	**2.0**	2.000	1249	1.39	11.00	0.0909	0.170	60.80	0.09	34.96	2.42	60.89	37.38	SPb-33
SPb-41	1370	2.0	**18.64**	**8.0**	2.999	1609	1.54	13.28	0.0753	0.180	59.02	0.41	33.86	2.65	59.43	36.51	SPb-41
SPb-46	1370	2.0	**20.24**	**4.5**	3.380	1670	*0.48*	*14.57*	0.0686	0.190	60.82	0.47	32.30	3.64	61.29	35.94	SPb-46
SPb-48	1420	2.5	**15.09**	**3.0**	2.758	1828	*0.39*	*14.54*	0.0688	0.190	60.15	0.43	32.97	2.88	60.58	35.86	SPb-48
SPb-55	1370	2.0	**11.86**	**3.6**	2.060	1736	*0.62*	*21.21*	0.0472	0.340	63.07	0.27	30.93	5.33	63.34	36.26	SPb-55

1 sigma standard error of sample glass 208/57 ranges from 0.2-3.4%, averages 1.5 %.

1 sigma standard error of sample suldide 208/57 ranges from 0.3-13.4%, averages 4.9 %.

Fe_2O_3 and FeO glass values are calculated from measured FeO total values.

Fe_2O_3 and FeO glass values in italics are calculated from maximum possible Delta FMQ.

See Appendix Table 1 for full major element data for both glass and sulfi

Table 2. Regresion Parameters for Kd versus 1/FeO Fits

Pressure GPa	Slope	±1sigma	Intercept	±1 sigma
1.0	479.7	28.6	-9.7	1.9
2.0	281.3	9.4	-1.0	1.2
2.5	190.9	82.1	1.4	6.7
2.5*	199.6	8.6	0.7	0.2
3.0**	162.4	3.8	1.4	0.3

X = 1/FeO; Y = Kd

* 2 GPa & 3 GPa intersection point used as a slope constraint, se

** includes run 24, corrected from 3.5 GPa to 3.0 GPa using our final parameterization.

Table 3. Cpx/Melt Partitioning of Pb

Clinopyroxene Pb = 5.76 ± 0.3 ppm (1σ)
Silicate glass Pb = 286.6 ± 4.3 ppm (1σ)
Kd cpx/melt = 0.0201 ± 0.0011 (1σ)

* Run SPb-12. 1370°C, 2.0 GPa, 24 hours.
* Major element analyses may be found in Table A.1.
* Above data are from a separate analysis than the sulfide-glass data in Table 1.

Table A.1. Electron Probe Analytical Data for Silicate Glass and Sulfide Melt Run Products

Run #	SiO2	TiO2	Al2O3	Cr2O3	FeO	MnO	MgO	CaO	Na2O	K2O	P2O5	NiO	S	Sum	Fe	Ni	Cu	Pb	S	O	Sum
	Silicate Glass														Sulfide Quenched Melt						
FeS															63.53				36.48		
ALV1690-20 *	49.77	1.696	15.4	0.038	10.04	0.171	7.61	10.93	3.049	0.134	0.202	0.023	**	99.07							
AII92-29-1 *	50.07	1.773	15.92	**	9.962	0.17	7.57	11.13	2.934	0.150	0.190	**	**	99.87							
SPb-2	46.09	1.680	14.73	0.000	12.50	0.233	9.01	10.22	3.398	0.271	0.218	0.019	0.442	98.80	57.43	1.074	0.193	7.488	34.83	3.837	103.73
SPb-2	46.29	1.703	14.82	0.042	12.48	0.187	8.94	10.01	3.160	0.277	0.225	0.025	0.422	98.57	55.77	1.071	0.190	5.255	35.42	3.691	102.51
SPb-4	45.08	1.630	14.17	0.033	17.09	0.167	6.77	9.65	3.004	0.121	0.165	0.629	0.004	98.52	4.32	####	0.050	1.179	19.04	0.383	103.51
SPb-5	47.12	1.685	14.72	0.040	15.28	0.166	6.98	10.07	2.872	0.126	0.152	0.160	0.039	99.41	17.19	####	0.076	0.597	27.57	0.690	103.41
SPb-9	48.34	1.650	14.72	0.035	13.29	0.139	6.93	9.93	2.749	0.118	0.167	0.017	0.130	98.22	62.42	0.200	0.094	1.968	35.08	2.861	102.62
SPb-11	43.58	0.996	9.34	0.054	36.80	0.084	2.78	4.96	1.115	0.083	0.143	0.057	0.450	100.44	68.07	0.299	0.103	0.609	30.37	2.885	102.19
SPb-12	46.69	1.456	12.74	0.019	4.75	0.120	12.34	15.31	2.188	0.129	0.171	0.016	0.081	96.00	64.21	0.205	0.109	2.057	32.87	1.094	100.54
SPb-13	48.74	1.703	15.03	0.034	11.00	0.176	7.39	10.65	2.840	0.139	0.175	0.014	0.157	98.05	61.28	0.189	0.106	1.998	34.84	2.854	100.79
SPb-15	49.57	1.720	15.41	0.035	9.05	0.143	7.29	10.72	2.940	0.161	0.175	0.009	0.158	97.62	68.50	0.156	0.091	1.650	30.33	1.143	101.86
SPb-19	48.08	1.696	15.03	0.035	11.84	0.148	7.21	10.34	3.000	0.155	0.167	0.005	0.170	98.13	61.14	0.080	0.222	1.995	34.85	2.096	100.38
SPb-24	35.51	0.950	9.30	0.042	39.91	0.138	4.54	6.12	1.554	0.089	0.143	0.021	0.625	98.93	71.83	0.112	0.182	0.571	25.41	1.661	99.76
SPb-32	47.61	1.606	15.05	0.110	12.64	0.138	7.04	10.10	3.046	0.147	0.199	0.680	0.150	97.72	61.54	0.270	0.612	2.049	34.89	2.521	101.88
SPb-33	47.64	1.554	14.92	0.340	12.25	0.13	7.39	10.22	2.901	0.129	0.200	0.680	0.170	97.50	60.80	0.089	0.146	2.000	34.96	2.420	100.41
SPb-41	46.61	1.516	14.54	0.260	14.66	0.134	7.15	9.79	2.869	0.136	0.182	0.720	0.179	97.77	59.02	0.411	0.678	2.999	33.86	2.647	99.61
SPb-46	46.45	1.517	14.45	**	15.00	0.132	7.10	10.15	2.867	0.133	0.188	**	0.192	98.17	60.82	0.466	0.406	3.380	32.30	3.636	101.01
SPb-48	46.01	1.496	14.36	**	14.89	0.132	7.05	9.60	2.807	0.133	0.192	**	0.187	96.85	60.15	0.432	0.332	2.758	32.97	2.884	99.53
SPb-55	41.91	1.403	13.18	0.006	21.77	0.133	6.59	9.94	2.664	0.133	0.187	**	0.338	98.25	63.07	0.267	0.175	2.060	30.93	5.328	101.83
SPb-12 Cpx	51.63	0.733	6.81	0.111	4.76	0.122	16.14	18.92	0.903	**	**	**	**	100.13							

All data is from electron microprobe except Pb in sulfide is LA-ICP-MS data. FeS is stoichiometric.
* MORB starting glasses
** Not analyzed for